Eur. Phys. J. A (2020) 56:24
https://doi.org/10.1140/epja/s10050-020-00021-2

THE EUROPEAN
PHYSICAL JOURNAL A

Special Article - New Tools and Techniques

A method to optimize mass discrimination of particles identified in ΔE–E silicon surface barrier detector systems

V. Scarduelli[1,2,a], **L. R. Gasques**[1], **L. C. Chamon**[1], **A. Lépine-Szily**[1]

[1] Instituto de Fisica, Universidade de Sao Paulo, Rua do Matao, 1371, Sao Paulo, SP 05508-090, Brazil
[2] Instituto de Física, Universidade Federal Fluminense, Niterói, RJ 24210-340, Brazil

Received: 26 September 2019 / Accepted: 26 November 2019 / Published online: 28 January 2020

Communicated by Maria Jose Garcia Borge

Abstract In several experiments, a system composed by two surface barrier detectors, one thin and one thicker, is used to identify the charge of a nucleus that is detected in this system. The nucleus loses part of its energy (ΔE) in the thin detector and the remaining part (E) is left in the thick one. Since the energy loss depends on the charge, this process allows the identification of the nuclear charge. The energy loss also depends on the mass of the particle, but with a lower degree of sensitivity. Therefore, the identification of the nuclear mass is much more difficult. In this paper, we present a method to treat the data in order to optimize the mass discrimination of particles detected in ΔE–E systems.

1 Introduction

The identification of charge, mass and energy of a nucleus is important in a large number of experiments and practical applications of nuclear physics. Different experimental devices can be used to determine each of these quantities individually. Other systems can be adopted for measurements of two or even three of these physical variables simultaneously.

ΔE–E detection systems are largely used in nuclear physics experiments to determine charge and energy of particles. There are different types of these systems. The basic principle of operation is the following. The nucleus first passes through a sufficiently thin detector, in which it loses only a fraction ΔE of its kinetic energy. Then it leaves the remaining energy (E) in the subsequent (thick) detector. The energy loss ΔE of the nucleus mainly depends on its energy and charge (for a review see *e.g.* [1,2]). Thus, the charge can be easily deduced from the ΔE and E measurements. ΔE also depends on the nuclear mass, but with much less sensitivity. Therefore, it is rather difficult to identify the mass of the nucleus from this type of measurement.

In gas-filled detectors, the energy loss is related to the interaction of the charged particle with the gas, while the remaining energy is measured by a thick detector placed at the end of the device [3–6]. Different types of gas detectors, such as ionization chambers, multiwire proportional chambers [7] and drift chambers [8] are available to fulfill particular experimental requirements. They offer some advantages such as flexibility in thickness, that can be varied according to the pressure of the gas, uniformity in the path length (related to the loss of energy resolution), immunity to radiation damage, etc. Most important, they present good energy loss resolution for heavy ions in the energy range of a few MeV/nucleon. However, in many situations, for improving the mass resolution of heavy charged particles, it is necessary to increase substantially the pressure of the gas. A possible gas leak may cause severe problems in the accelerator during an experiment. To avoid this problem, thick windows should be used to separate the gas recipient from the high vacuum of the scattering chamber. The straggling in the window may worse the resolution of the total energy of the particles. An important disadvantage of this kind of system lies in the fact that most of the gaseous detectors presents a design that occupies a large volume, which can be a drawback in experiments where simultaneous measurements are performed for several angles (requiring several detector systems).

In order to improve the mass resolution, time-of-flight (TOF) measurements are often performed in experiments with heavy ions [9,10]. The corresponding technique is based on the determination of two quantities: energy of the particle and time interval spent by the particle to travel a certain path length. Usually, the stopping time signal is given by the same detector used to measure the energy. Concerning the starting time signal, there are basically two types of TOF systems: (i) it is related to the frequency of a pulsed beam of the accel-

---

[a] e-mail: scarduelli@gmail.com

erator; (ii) it is obtained using a foil or a detector placed at the beginning of the path. Not all accelerator facilities have the capability of producing pulsed beams. In general, foils or detectors used to generate the starting signal cause some spread of the energy resolution. The mass resolution is related to the traveling time of the particle, which depends on the path length. Therefore, to achieve a good mass resolution, this kind of device normally occupies a large space, which might result in a similar issue of having a setup constructed with gaseous detectors.

In contrast with gas-filled detectors and TOF devices, telescopes where both ΔE and E signals are obtained with semiconductor detectors can be quite compact. For this reason, modern arrays consisting of many of these (or segmented) ΔE–E telescopes are frequently used to investigate angular distributions of heavy ion reactions (see e.g. [11]).

In the present work, we deal with telescopes in which both signals, ΔE and E, arise from silicon surface barrier semiconductor detectors. As commented above, it is rather difficult to identify the mass of the nucleus from this type of measurement. Therefore, we have developed a method of data treatment to optimize the mass discrimination of particles identified in ΔE–E surface barrier telescopes, which is described in the present paper.

2 The experiment

The experiment was carried out at the Open Laboratory of Nuclear Physics (LAFN, acronym in Portuguese) of the University of São Paulo. Making use of the Pelletron 8MV accelerator, we obtained beams of several nuclei: ^{6}Li, ^{7}Li, ^{12}C, ^{16}O, ^{19}F, ^{28}Si, ^{35}Cl, at different energies. Since in this work the lithium isotopes are chosen as example to illustrate the method for mass discrimination, measurements were performed in steps of 1 MeV in the energy range from $E_{Lab.} = 19.4$ MeV to 28.4 MeV for ^{6}Li, and from 20.0 MeV to 28.0 MeV for ^{7}Li. The projectiles were scattered by a quite thin (about 7 μg/cm^2) ^{197}Au target evaporated on a ≈ 10 μg/cm^2 carbon backing. The products of the collisions were detected in a ΔE–E telescope placed at $\theta_{Lab.} = 60°$. Our analyzes are focused on the elastic scattering of the projectiles on ^{197}Au. Therefore, the kinetic energy of the detected projectile is well known since it is determined by kinematics. Although small, the (average) energy loss of the projectiles in the target has been taken into account in our calculations. In addition, as a complement to the experiment, we have also used an alpha source, composed of ^{230}Th, ^{241}Am and ^{244}Cm, placed in front of the ΔE–E telescope (without target), in order to obtain measurements of ^{4}He at different energies.

A schematic view of the detection system is presented in Fig. 1. The nucleus with total kinetic energy E_T passes through the first (thin) detector, that provides the ΔE signal, and stops in the second (thick) detector (E signal). The ΔE detector used in our experiment is from `ORTEC`, has an active area of 50 mm^2 and thickness of $\varepsilon = 14.6$ μm. The E detector is from `CANBERRA`, has an active area of 150 mm^2 and thickness of $\varepsilon = 500$ μm. Both detectors have thin coverage layers (see Fig. 1). According to the specifications, the electrode thickness of the ΔE detector corresponds to 40.4 μg/cm^2 of gold placed in one side, and 40.6 μg/cm^2 of aluminum on the other side, while the E detector has a quite thin entrance window with thickness of about 0.05 μm equivalent silicon. Since the energy resolution is quite important in the experiment, the average energy loss of the nuclei in the coverage layers of the detectors was taken into account in our analyzes.

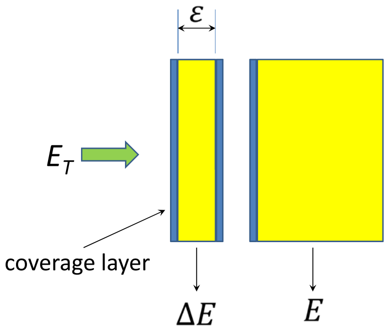

Fig. 1 (Color online) Schematic view of the detection system. A nucleus with total kinetic energy E_T is detected in the telescope, which produces the ΔE and E signals. The sensitive thickness of the ΔE detector is ε. One of the coverage layers of the detectors is indicated with an arrow in the figure

We took great care to perform quite accurate calibrations of both detectors. In order to calibrate detector E, part of the experiment was performed without mounting the ΔE detector on the telescope. With this, the energy of the nucleus hitting the detector E is determined by the kinematics (with a small correction due to the small energy loss in the target and in the detector entrance layer). Therefore, it is known with high precision. Figure 2 shows the results for the calibration of detector E obtained with different projectiles, including those from the alpha source.

The calibration of detector ΔE was performed by scattering beams corresponding to the heaviest projectiles of our experiment: ^{19}F, ^{28}Si and ^{35}Cl. Due to their large charge, these projectiles do not pass through detector ΔE, but actually stop at this detector. With this, the corresponding energy supplied to the detector is very well known, which allows accurate calibration. The alpha source emits particles at (a few) discrete energies, which do not stop at the ΔE detector. These alpha particles lose little energy in the detector ΔE, and thus allow accurate determination of the slope of the calibration when considered in conjunction with the data of the heaviest projectiles. Therefore, data obtained with the

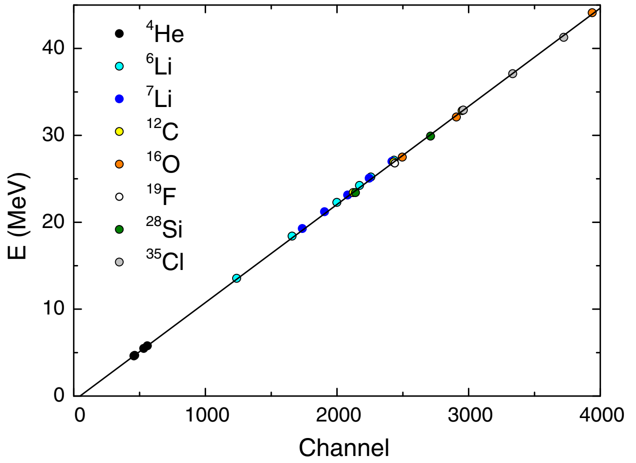

Fig. 2 (Color online) Energy versus channel obtained with different beams in the process of calibration of detector E. The continuous line represents the linear fit of the collected data

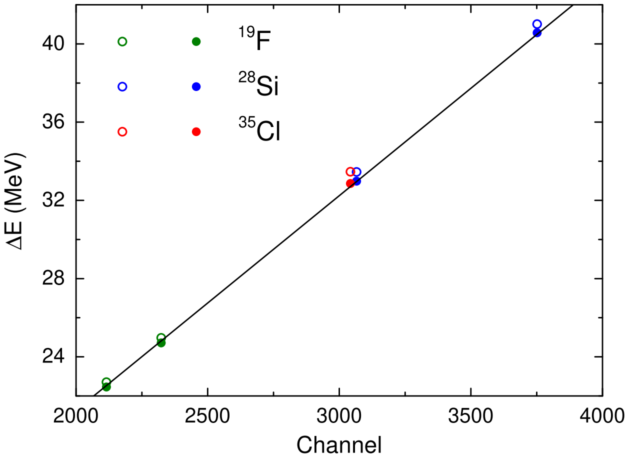

Fig. 3 (Color online) Energy versus channel obtained with different beams in the process of calibration of detector ΔE. The closed and open circles represent the energy of the nucleus, with and without correction due to the energy loss (in the target and entrance coverage layer), respectively. The data from alpha source are not presented in the figure

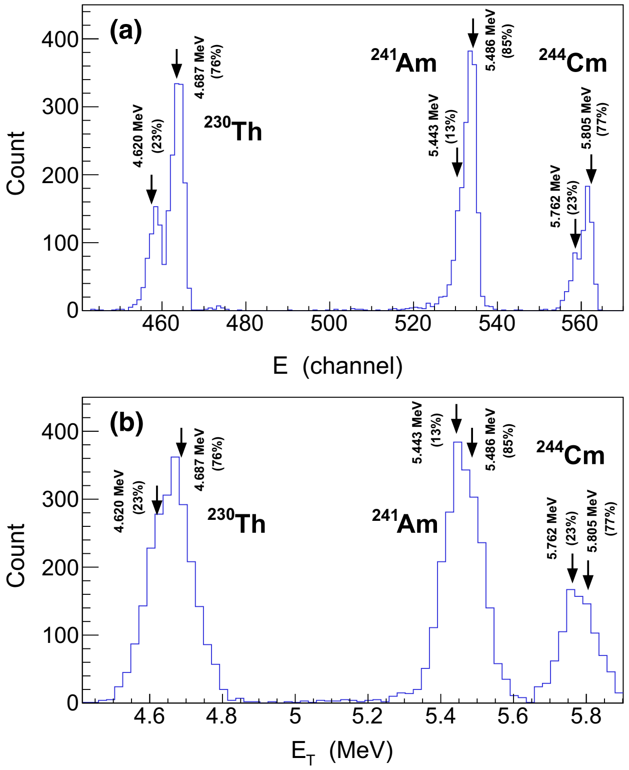

Fig. 4 (Color online) **a** Single-channel energy spectrum obtained with the alpha source incident directly on the detector E. The arrows indicate different energies of the alpha particles (see text for details). **b** Projection of the ΔE–E_T spectrum of Fig. 5b on the total kinetic energy axis, resulting in a single-channel spectrum of the type: count versus E_T

alpha source were also used in the calibration of detector ΔE. In this process, as the total kinetic energies of the alpha particles are known, the energy loss in detector ΔE was obtained considering the remaining energy in detector E (through its calibration), and assuming calculated energy loss in the outer layers of detector ΔE. In Fig. 3, we present the high energy part of the ΔE detector calibration. The closed and open circle symbols in this figure represent the energy of the elastically scattered projectile, with and without correction corresponding to the energy loss (in the target and in the ΔE detector entrance coverage layer), respectively. We emphasize that the correction due to the energy loss (in the target and coverage layer) is important (and should be taken into account) especially in cases involving heavy nuclei.

Figure 4a shows a single-channel spectrum (counting as a function of energy, displayed in channel unit) obtained with the alpha source directly facing the detector E (obtained without mounting the detector ΔE). We can observe several peaks corresponding to different energies of alpha particles that come from the isotopes present in the source: ^{230}Th, ^{241}Am and ^{244}Cm. The energy resolution of this detector is quite good ($\frac{\mathrm{FWHM}}{\mathrm{Centroid}} \approx 0.7\%$) and allows clear identification of the two peaks from ^{230}Th separated by only about 60 keV (see Fig. 4a)

Figure 5a shows a ΔE–E spectrum obtained with the alpha source directly incident on the complete telescope. The ΔE and E axes are displayed in MeV units, obtained with the respective calibrations. Figure 5b shows the same data, but now in the form of a ΔE–E_T spectrum, where the total kinetic energy E_T was obtained by summing the energy loss ΔE with the residual energy E.

The window drawn with black lines in Fig. 5a delimits a region of events that correspond to alphas coming only from ^{230}Th present in the source. The red line shown in this figure represents the function: $\Delta E + E = E_T =$ constant, where the constant 4.67 MeV is the weighted average value of the two energies of the alpha particles emitted by ^{230}Th.

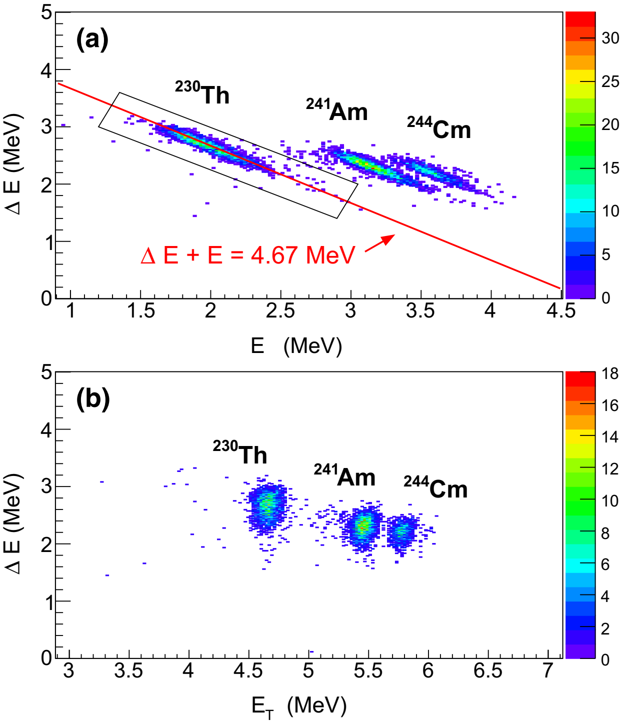

Fig. 5 (Color online) **a** ΔE–E and **b** ΔE–E_T spectra obtained with the alpha source. The scales of colors at the right side of the figure are related to the number of events detected

There are many events detected along this line with some dispersion in relation to the axis of energy loss. This is an expected behavior since the energy loss of the particles in the ΔE detector is a random process with statistical dispersion. As the mass identification obtained with ΔE–E measurements is related to the energy loss, the mass resolution depends strongly on the dispersion of the ΔE signal. Therefore, we have investigated this dispersion in detail, as follows.

In order to check whether the observed experimental ΔE dispersion is consistent with theoretical models of energy loss, we performed Monte Carlo calculations using the TRIM code [2,12–14], concerning to energy loss of alpha particles that pass through the detector ΔE. In these calculations, we considered alpha particles with total kinetic energies of 4.620 MeV (23.5% of events) and 4.687 MeV (76.5%), thus simulating alphas coming from ^{230}Th, and adopted the detector specifications as described above. The results of these calculations are presented in Fig. 6, where the blue line represents the distribution of probability (in arbitrary units) for the energy loss. With the purpose of comparison, the histogram in this figure corresponds to the experimental results obtained with the projection of events that are inside the window shown in Fig. 5a on the ΔE axis. As shown in Fig. 6, the experimental dispersion is about three times larger than the theoretical prediction. One reason for this difference may be related to small variations of the thickness of the detector ΔE. To illustrate this, we performed other Monte Carlo simulations, increasing and decreasing the detector thickness by about 5%. The corresponding results are shown by green and red lines in Fig. 6. Clearly, a 5% variation in the detector thickness would reproduce the experimental dispersion observed for ΔE. Note that part of this effect may be related to the intrinsic variation of thickness of the detector, and part could originate from the angular aperture of the collimator system, since small differences in the angle of incidence on the detector result in different path lengths of the particles inside the detector. Therefore, the angular collimator system has significant influence on the mass resolution that is obtained in this type of experiment. The present measurements were performed with an angular aperture of $\Delta\theta \approx \pm 1.7°$, corresponding to a dispersion of about 3% in the path length.

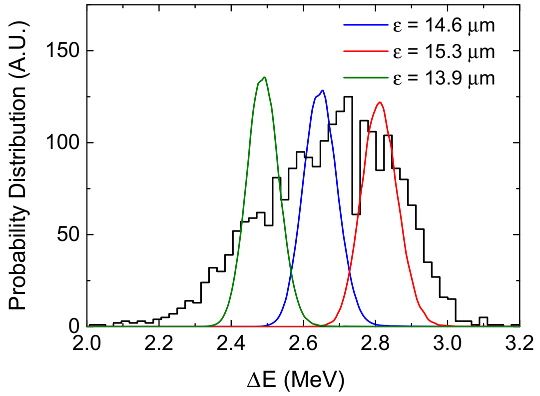

Fig. 6 (Color online) The histogram in the figure represents the projection of events that are inside the window shown in Fig. 5a on the ΔE axis. The lines represent theoretical probability distributions (in arbitrary units) for the energy loss of alpha particles passing through the detector ΔE, considering different thicknesses for this detector

In Fig. 4b, we present a projection of the ΔE–E_T spectrum of Fig. 5b on the E_T axis of the total kinetic energy. It is clear that the resolution in this case is worse than that presented in Fig. 4a, although both represent energy results for the same alpha source. In fact, in one case E_T is obtained from the composition of the results of two (E and ΔE) detectors (and electronics), while in the other case E_T is measured directly by only one (E) detector. Thus, the presence of the detector ΔE in the telescope allows to obtain information about the nuclear charge (and mass), but worsens the resolution related to the total kinetic energy.

3 A method to treat the data

In Fig. 7a, we present a ΔE–E_T spectrum that involves the sum of all the results obtained with different projectiles and bombarding energies of our experiments. The vast majority of these events come from the elastic scattering of the projectiles on the ^{197}Au target, since the bombarding energies of

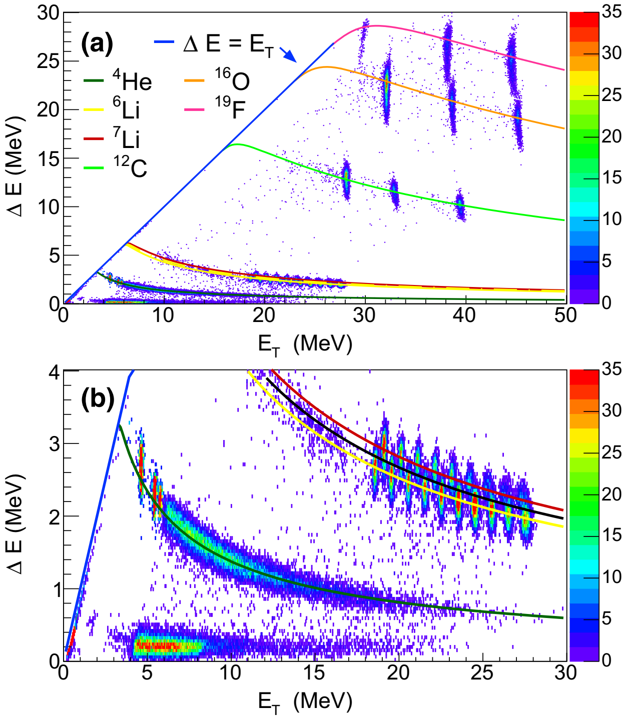

Fig. 7 (Color online) **a** ΔE–E spectrum involving the sum of all results obtained with different projectiles and bombarding energies from our experiments. The lines represent theoretical calculations for energy loss of each projectile in detector ΔE. **b** The same spectrum of part (**a**), but now expanded to show the region of the lithium isotopes

the experiments are well below the Coulomb barrier for these systems. The lines in the figure represent theoretical calculations of (average) energy loss for each projectile (indicated by different colors in the figure) in the detector ΔE, as a function of the total energy (at the entrance of this detector). These numerical calculations were performed according to the code reported in [15]. The line indicated with a blue arrow represents the function $\Delta E = E_T$, in which case the nucleus would stop inside the detector ΔE. Figure 7b shows the same spectrum, but this time expanded in the region of the lithium isotopes and helium. It is interesting to note that many events detected in the ^{4}He region did not arise from the alpha source, but they actually came from nuclear reactions originated through other projectiles interacting with the target. Also some events of ^{6}Li and ^{7}Li arise from nuclear reactions involving other projectiles.

Clearly, as shown in Fig. 7a, the identification of the nuclear charge with this experimental arrangement is an easy task. The same can not be said for the nuclear mass, since the energy loss does not depend strongly on it (see the ^{6,7}Li region in Fig. 7b). Thus, it is desirable to have a method of data processing that optimizes mass discrimination.

The correct quantum-mechanical calculation for the mean energy loss per distance of charged particles passing through matter was first performed by Hans Bethe [16]. For low energies (which is the case of the present work), the Bethe formula reduces to:

$$-\frac{dE_T}{dx} = \frac{\eta e^4}{2\pi\epsilon_0^2}\,\frac{Z^2 M}{E_T m_0}\ln\left(\frac{4m_0 E_T}{M\,I}\right), \tag{1}$$

where η is the electron density of the material, m_0 is the mass of the electron, Z is the number of protons of the particle, M is its mass and E_T its energy. The I parameter in Eq. (1) represents the mean excitation potential, for which Felix Bloch [17] proposed that:

$$I \approx z \times 11\,eV, \tag{2}$$

where z is the atomic number of the material. If one neglects the slow variation (with E_T/M) of the logarithm term in Eq. (1), the mean loss of energy of a particle in a given material (^{28}Si in our case) of thickness ε is given by:

$$\Delta E \approx C\,\varepsilon\,\frac{MZ^2}{E_T}, \tag{3}$$

where C is approximately constant. To obtain (3), we used $dx \to \varepsilon$ in Eq. (1) and, therefore, ε should not be large. If Eq. (3) were applicable, a ΔE–E_T spectrum could be easily transformed into a mass-E_T spectrum, by association of the mass with the energy loss through:

$$M = \frac{E_T}{Z^2\,C\,\varepsilon}\,\Delta E. \tag{4}$$

However, this equation is a too crude approximation and is not appropriate to be applied (with precision) in the linearization of spectra like that presented in Fig. 7.

In order to illustrate the last statement, in Fig. 8a we present the same data of Fig. 7b, but now the ordinate axis represents the product $\Delta E \times E_T$ (instead of ΔE in Fig. 7). According to Eq. (4), the quantity $\Delta E \times E_T$ should be proportional to the mass of the particle. The black line in Fig. 8b represents a projection of the events inside the rectangle drawn in Fig. 8a over the $\Delta E \times E_T$ axis. The events in this rectangle correspond to ^{6}Li and ^{7}Li nuclei. The histogram of Fig. 8b does not indicate any separation between these two mass numbers.

Since we have used different beams in our experiment, we can separate the contributions of ^{6}Li and ^{7}Li. The green and red lines in Fig. 8b represents the contribution of these isotopes. With this, we can provide a quantitative evaluation of the mass resolution, through the figure of merit M:

$$M = \frac{|\mathrm{C}_1 - \mathrm{C}_2|}{\mathrm{FWHM}_1 + \mathrm{FWHM}_2}, \tag{5}$$

where C_1 and C_2 represent the centroids of both peaks, FWHM_1 and FWHM_2 are the corresponding full widths at half maximum. According to [18], $M \geq 2$ indicates quite good resolution, while $M \leq 0.5$ indicates that there is no separation between the peaks. In the case commented above, we obtained $M = 0.38$.

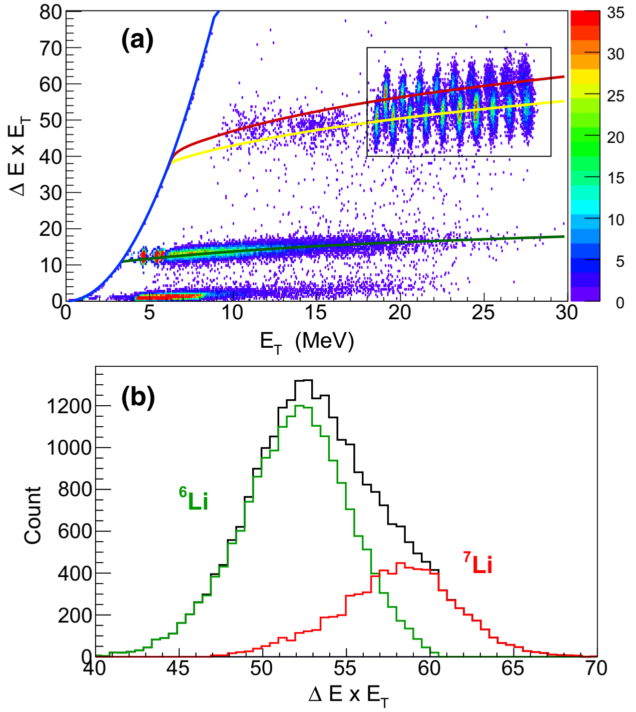

Fig. 8 (Color online) **a** The same as Fig. 7b, but now the ordinate axis corresponds to $\Delta E \times E_T$ values. **b** The histogram in black line represents the number of events contained inside the rectangle of part (**a**), as a function of the $\Delta E \times E_T$ value. The green and red lines are the contributions of each isotope

The red and yellow lines in Fig. 8a represent realistic calculations of loss of energy as a function of the total energy for ^{6}Li and ^{7}Li. Clearly, the trend of these lines is not orthogonal to the $\Delta E \times E_T$ axis, meaning that $\Delta E \times E_T$ is not constant (proportional to the mass) as indicated by Eq. (4) (or (3)). In fact, Eq. (3) is appropriate to describe the energy loss only in a region of total energy much higher than that involved in the present experiment.

In this work, we propose a method to process the data with the aim of optimizing the mass discrimination in this kind of ΔE–E experiment. In our procedure, we do not adopt Eq. (4), but we still suppose that the loss of energy is approximately proportional to the mass. As an example, we apply the method in the present case for the lithium isotopes. The black line in Fig. 7b represents the average value for the mean energy loss of the two lithium isotopes, as a function of the total energy. The idea is to use these theoretical results for the average energy loss in order to linearize the data obtained for ^{6}Li and ^{7}Li, and project them over a "mass" axis, according to the following procedure:

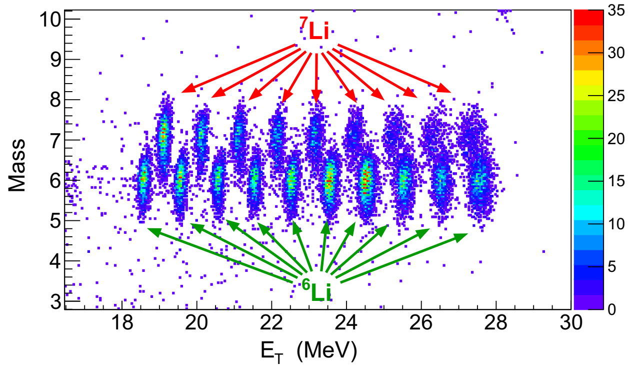

Fig. 9 (Color online) Mass-E_T spectrum obtained with our data according to the procedure described in the text

1. For each detected event, we know the corresponding energy loss and total energy obtained making use of the calibration of the detectors. We call these as the experimental ΔE and E_T values.
2. With the experimental E_T value, we obtain the respective theoretical average energy loss $\langle \Delta E \rangle$ through the (numerical) function represented by the black line in Fig. 7b.
3. Then we obtain the "mass channel", which we define as:

$$mass = K \times \frac{\Delta E}{\langle \Delta E \rangle}, \tag{6}$$

   where K is a constant that represents the average mass of the isotopes. In the present case $K = 6.5$.
4. Considering the complete set of events, we then are capable to obtain a mass-E_T spectrum, as that presented in Fig. 9. In this controlled experiment, we know what events are associated to each lithium isotope. Thus, we have indicated by arrows in Fig. 9 the regions that correspond to ^{6}Li and ^{7}Li. Of course, in a practical application this identification could not be done *a priori*.

As a result of the method explained above, we linearized the data shown in Fig. 7b in relation to the mass axis, as can be observed in Fig. 9. Events corresponding to the lithium isotopes (which are the ones chosen as example) are approximately positioned on a line perpendicular to the mass axis (ordinate). The assumption used for linearization corresponds to Eq. (6), where the theoretical energy loss $\langle \Delta E \rangle$ should be calculated with realistic models. With this, the method is quite general and can be applied in different experimental conditions (energy range, thickness of the detector, etc).

As a final step of our method, we project the mass-E_T spectrum on the mass axis, as illustrated in Fig. 10a. In part (b) of this figure, we show contributions of each isotope separately (through different colors). The figure of merit has improved significantly: $M = 0.75$. In practical applications, where the separation of isotopes could not be done a priori, the analysis of a spectrum like that of Fig. 10a would provide the contributions corresponding to each isotope. In addition, the study could also be performed as a function of the energy.

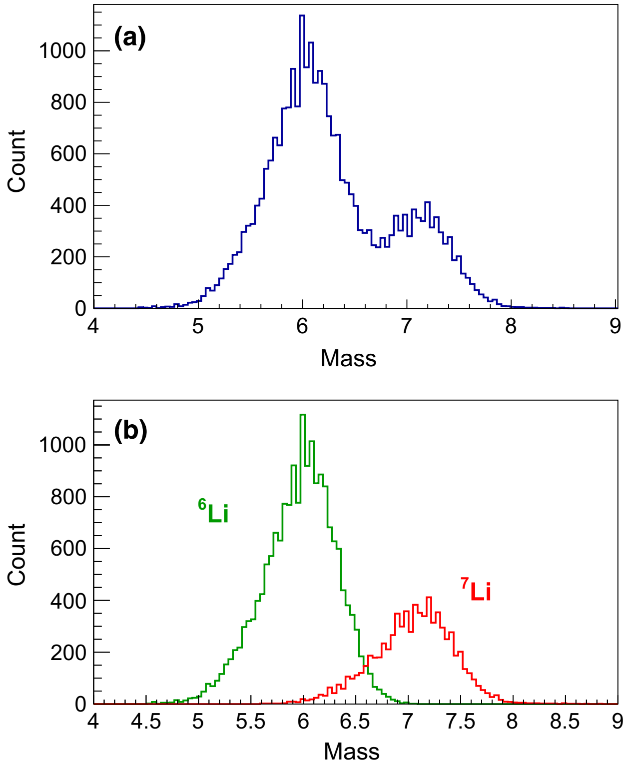

Fig. 10 (Color online) **a** Projection on the mass axis of the mass-E_T spectrum presented in Fig. 9. **b** Contributions of ^{6}Li and ^{7}Li

For instance, we could make a projection on the mass axis of events contained only inside a window drawn in Fig. 9. In this case, we would discriminate mass for events contained within a limited range of total energy.

4 Conclusion

The mass resolution obtained in experiments involving ΔE–E measurements depends on several features of the experimental apparatus: the energy resolution of the detector E, the average thickness of the detector ΔE, the intrinsic variation of the thickness of the detector ΔE, the angular aperture of the collimator system, etc. In this type of experiment, it is important to treat the data as well as possible in order to optimize the mass resolution. In the present paper, we presented a method with this purpose. The method demands previous realistic calculations of energy loss in the detector ΔE as a function of the total kinetic energy of the particles. These theoretical results are used with the purpose of linearizing the data, obtaining a mass-E_T spectrum. The projection of the data, with or without windows limiting the energy range, provides a form to estimate the contribution of different isotopes. A comparison between the results presented in Figs. 8b and 10a clearly illustrates the great improvement in mass discrimination obtained with the present proposed procedure in relation to other usual methods.

Acknowledgements This work has been partially supported by Fundação de Amparo à Pesquisa do Estado de São Paulo (FAPESP) Proc. No 2018/09998-8, Conselho Nacional de Desenvolvimento Científico e Tecnológico (CNPq) Proc. No 407096/2017-5, and it is a part of the project INCT-FNA Proc. No 464898/2014-5.

Data Availability Statement This manuscript has no associated data or the data will not be deposited. [Authors' comment: The data set used in this work corresponds to the spectrum shown in the figures.]

References

1. W.R. Leo, *Techniques for Nuclear and Particle Physics Experiments* (Springer, New York, 1994)
2. J.F. Ziegler, J. Biersack, U. Littmark, *The Stopping and Range of Ions in Matter* (Pergamon Press, Oxford, 1985)
3. M.M. Fowler, R.C. Jared, A gas ionization counter for particle identification. Nucl. Instrum. Methods **124**, 341 (1975)
4. P. Gässel, R.C. Jared, L.G. Moretto, Identification of atomic numbers up to Z=60 by means of $\Delta E-E$ telescopes and a computerized method. Nucl. Instrum. Methods **142**, 569 (1977)
5. Y. Yoshida, K. Tsuji, F. Toyofuku, A. Katase, Ionization chamber telescopes for position determination and nuclear charge identification of fission fragments. Nucl. Instrum. Methods **159**, 125 (1979)
6. M.N. Rao, D.C. Biswas, R.K. Choudhury, Charge determination of fission fragments via energy loss and X-ray measurements. Nucl. Instrum. Methods Phys. Res. B **51**, 102 (1990)
7. G. Charpak, Evolution of the automatic spark chambers. Ann. Rev. Nucl. Sci. **20**, 197 (1970)
8. A.H. Walenta, J. Heintze, B. Schürlein, The multiwire drift chamber a new type of proportional wire chamber. Nucl. Instrum. Methods **92**, 373 (1971)
9. P. Håkansson, An introduction to the time-of-flight technique. Braz. J. Phys. **29**, 422 (1999)
10. D.H. Luong, M. Dasgupta, D.J. Hinde, R. du Rietz, R. Rafiei, C.J. Lin, M. Evers, A. Diaz-Torres, Predominance of transfer in triggering breakup in sub-barrier reactions of ^{6,7}Li with ^{144}Sm, ^{207,208}Pb, and ^{209}Bi. Phys. Rev. C **88**, 034609 (2013)
11. S. Kalkal et al., Asymptotic and near-target direct breakup of ^{6}Li and ^{7}Li. Phys. Rev. C **93**, 044605 (2016)
12. J.F. Ziegler, "SRIM-2003", Nucl. Instrum. Methods Phys. Res. B **219**, 1027 (2004)
13. J.F. Ziegler, J.P. Biersack, M.D. Ziegler, *SRIM—The stopping range of ions in matter* (SRIM Co., 2008)
14. J.F. Ziegler, M.D. Ziegler, J.P. Biersak, SRIM–The stopping and range of ions in matter. Nucl. Instrum. Methods Phys. Res. B **268**, 1818 (2010)
15. A. Schinner, P. Sigmund, Expanded PASS stopping code. Nucl. Instrum. Methods Phys. Res. B **460**, 19 (2019)
16. H. Bethe, Zur Theorie des Durchgangs schneller Korpuskularstrahlen durch Materie. Ann. Phys. **397**, 325 (1930)
17. F. Bloch, Zur Bremsung rasch bewegter Teilchen beim Durchgang durch Materie. Ann. Phys. **408**, 285 (1933)
18. R.A. Winyard, J.E. Lutkin, G.W. McBeth, Pulse shape discrimination in inorganic and organic scintillators. Nucl. Instrum. Methods **95**, 141–153 (1971)